



# Heat-induced planar shock waves in supercritical fluids

M. T. Migliorino<sup>1,2</sup> · C. Scalo<sup>3</sup>

Received: 2 February 2019 / Revised: 31 October 2019 / Accepted: 6 December 2019

© Springer-Verlag GmbH Germany, part of Springer Nature 2019

## Abstract

We have investigated one-dimensional compression waves, produced by heat addition in quiescent and uniform initial conditions, in six different supercritical fluids, each taken in four states ranging from compressible pseudo-liquid fluid to ideal gas. Navier–Stokes simulations of a canonical semi-infinite domain flow problem, spanning five orders of magnitude of heating rate, are also carried out to support the theoretical analysis. Depending on the intensity of the Gaussian-shaped energy source, linear waves or shock waves due to nonlinear wave steepening are observed. A new reference heating rate parameter allows to collapse in the linear regime the whole dataset, together with the existing experimental data, thanks to its absorption of real-fluid effects. Moreover, the scaling strategy illustrates a clear separation between linear and nonlinear regimes for all fluids and conditions, offering motivation for the derivation of a unified fully predictive model for shock intensity. The latter is performed by extending the validity of previously obtained theoretical results in the nonlinear regime to supercritical fluids. Finally, thermal to mechanical power conversion efficiencies are shown to be proportional, in the linear regime, to the fluid's Grüneisen parameter, which is the highest for compressible pseudo-liquid fluids, and maximum in the nonlinear regime for ideal gases.

**Keywords** Scaling · Blast waves · Supercritical fluids · Heat addition · Peng–Robinson EoS · Navier–Stokes equations

## 1 Introduction

When compressible fluids are thermally perturbed, a mechanical response is generated in the form of waves [1,2], which can range in intensity from acoustic compressions [3] to shock waves [4]. Heat-induced waves appear in a wide variety of natural and artificial phenomena, such as the sound produced from asteroids' impact on Earth's atmosphere [5,6], blast waves from nuclear explosions [7], thermo-

phones [8], shock waves induced by spark discharge [9], thunder [10], and space manufacturing processes [11]. Moreover, heat-induced fluctuations, referred to by some authors as thermoacoustic waves [12,13] or thermoacoustic sound [8], are the governing mechanism for thermal relaxation in near-critical fluids in enclosed cavities [14–20]. This phenomenon, referred to as the piston effect [16] or thermoacoustic convection [21], has been widely investigated through numerical simulations [13,22–24] and experiments [3,21,25,26].

In spite of such efforts, fully predictive models for heat-induced wave intensity in supercritical fluids have been limited to low-amplitude acoustic waves [3], with less attention devoted to shock waves. Moreover, the previously reported scaling relationships for heat-induced waves [27] fail in the case of supercritical fluids, because of the lack of consideration for real-fluid effects in the selection of the reference heating rate parameter. Furthermore, an open fundamental question is whether supercritical fluids guarantee higher heat to mechanical power conversion efficiency with respect to ideal gases. Given the wide interest of the scientific community in non-ideal compressible fluid dynamics,

---

Communicated by M. Brouillette.

✉ M. T. Migliorino  
mariotindaro.migliorino@uniroma1.it

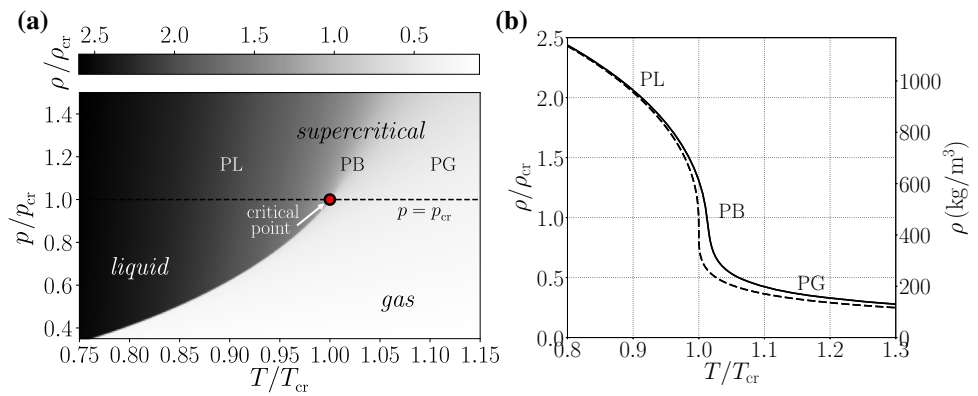
C. Scalo  
scalo@purdue.edu

<sup>1</sup> School of Mechanical Engineering, Purdue University, West Lafayette, IN 47907, USA

<sup>2</sup> Present Address: Department of Mechanical and Aerospace Engineering, Sapienza University of Rome, via Eudossiana 18, 00184 Rome, Italy

<sup>3</sup> School of Mechanical Engineering, and Aeronautical and Astronautical Engineering (by courtesy), Purdue University, West Lafayette, IN 47907, USA

**Fig. 1** **a** Phase diagram of CO<sub>2</sub> showing flooded contours of reduced density  $\rho/\rho_{cr}$ ; **b** reduced density of CO<sub>2</sub> versus reduced temperature  $T/T_{cr}$  for  $p = p_{cr}$  (dashed line) and  $p = 1.1 p_{cr}$  (solid line). Both plots are generated with the Peng–Robinson equation of state. PL, PB, and PG indicate pseudo-liquid, pseudo-boiling, and pseudo-gaseous conditions, respectively



especially in shock waves [28–32], it is desirable to address the aforementioned literature gaps.

The present manuscript is structured as follows. The problem under consideration is formulated in Sect. 2, with the selection of thermodynamic states and fluids of interest in Sect. 2.1 and the description of the governing equations and of the computational setup in Sect. 2.2. The results section (Sect. 3) covers: (1) the linear regime of heat-induced waves (Sect. 3.1), where the new reference heating rate parameter is proposed; (2) the nonlinear regime (Sect. 3.2), where wave steepening is followed by the formation of shock waves, the amplitude of which is accurately predicted with a new model; and (3) the analysis of thermal to mechanical power conversion efficiency (Sect. 3.3). Finally, the manuscript’s main findings are summarized in Sect. 4.

## 2 Problem formulation

### 2.1 Fluid model

Hereafter, we refer to supercritical fluids as fluids pressurized above their critical point,  $p > p_{cr}$  (Fig. 1a), indicated by the subscript cr. Such fluids exhibit variations in density, speed of sound, and thermal capacity, ranging from liquid-like to gas-like values depending on their temperature, making them an attractive choice for the scope of the present investigation. In fact, for a given supercritical pressure (chosen as  $p_0 = 1.1 p_{cr}$  in this study), starting from cold and heavy pseudo-liquid conditions (PL, for  $T < T_{cr}$ ), the density rapidly drops for increasing temperatures (Fig. 1b) via a pseudo-boiling (PB), or pseudo-phase transitioning, process [33–35], after which the fluid reaches a pseudo-gaseous (PG) state, and then eventually a near-ideal-gas (IG) state for sufficiently high temperatures. This behavior can be captured by adopting analytically defined equations of state for real fluids, which enable a thermodynamically consistent closure of the governing flow equations.

**Table 1** Marker legend for the selected six fluids, each considered in four different supercritical thermodynamic states represented by grayscale levels

Fluid	PL	PB	PG	IG	$T_{cr}$ (K)	$p_{cr}$ (MPa)
CO <sub>2</sub>	●	●	○	○	304.13	7.3773
O <sub>2</sub>	▲	▲	△	△	154.58	5.043
N <sub>2</sub>	▼	▼	▽	▽	126.20	3.398
CH <sub>3</sub> OH	■	■	□	□	512.64	8.097
R-134a	◆	◆	◇	◇	374.26	4.059
R-218	◆	◆	◇	◇	345.10	2.68
$T_0/T_{cr}$	0.89	1.02	1.11	2.20		
$p_0/p_{cr}$	1.1	1.1	1.1	1.1		

Black: pseudo-liquid fluid (PL); dark gray: pseudo-boiling (PB) fluid; light gray: pseudo-gaseous (PG) fluid; white: fluid near to ideal-gas (IG) conditions. Such reference conditions are indicated with the subscript 0 and are used as initial conditions. All cases are considered at  $p_0 = 1.1 p_{cr}$ . Values of fluid-specific critical properties ( $T_{cr}$ ,  $p_{cr}$ ) [36,37] are also reported

The fluids considered in this study (Table 1) are: carbon dioxide (CO<sub>2</sub>), oxygen (O<sub>2</sub>), nitrogen (N<sub>2</sub>), methanol (CH<sub>3</sub>OH), 1,1,1,2-tetrafluoroethane (CH<sub>2</sub>FCF<sub>3</sub> or R-134a), and octafluoropropane (R-218). The Peng–Robinson equation of state [38], hereinafter called PR EoS, is chosen for the present investigation because of its simplicity and acceptable accuracy for the range of flow conditions considered. A Newton–Raphson-based iterative method is employed to obtain temperature from density and internal energy. Real-fluid dynamic viscosity and thermal conductivity are estimated via Chung et al.’s method [39], whose accuracy only affects the simulation of thermoviscous processes (see appendix of [40]). However, the jumps of the thermo-fluid-dynamic quantities across the shocks as well as the profiles of the compression waves in the isentropic wave propagation regime—both comprising the focus of the present manuscript—are independent from the values of viscosity and conduction coefficient. The prediction and analysis of the details of the shock profile structure is out of the scope of this work.

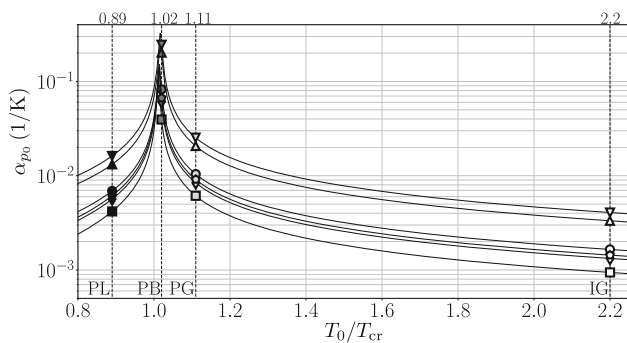


**Fig. 2** Isobaric thermal expansion coefficient (1) versus reduced temperature obtained through the PR EoS. The symbols correspond to the fluids and conditions in Table 1

The isobaric thermal expansion coefficient (Fig. 2),

$$\alpha_p = -\frac{1}{\rho} \left( \frac{\partial \rho}{\partial T} \right)_p, \tag{1}$$

is the thermodynamic variable of choice to guide the selection of the different base conditions shown in Table 1: state in the pseudo-boiling (PB) region, in the immediate vicinity of the maxima of  $\alpha_p$  ( $T_0 = 1.02T_{cr}$ ), state in the pseudo-liquid region (PL,  $T_0 = 0.89T_{cr}$ ), and state in the pseudo-gaseous region (PG,  $T_0 = 1.11T_{cr}$ ). For the ideal-gas (IG) region, we choose the state at  $T_0 = 2.2T_{cr}$ , for which  $\alpha_{p0}T_0 \approx 1$ . The IG state is thus modeled with the perfect ideal-gas EoS,  $p = \rho RT$ , and with a constant ratio of specific heats  $\gamma$ , taken equal to the ratio of  $c_p$  and  $c_v$  given by the PR EoS at  $T = 2.2T_{cr}$  and  $p = 1.1p_{cr}$ .

The selection in Table 1 results in a total of 24 distinct thermodynamic initial states, spanning an overall pressure, temperature, and density range, respectively, of approximately  $p_{0,max} - p_{0,min} = 6$  MPa,  $T_{0,max} - T_{0,min} = 1016$  K, and  $\rho_{0,max} - \rho_{0,min} = 1340$  kg/m<sup>3</sup>.

## 2.2 Governing equations and computational setup

The governing equations for a fully compressible one-dimensional viscous flow read

$$\frac{\partial \mathbf{C}}{\partial t} + \frac{\partial \mathbf{F}}{\partial x} = \mathbf{S}, \tag{2}$$

where  $\mathbf{C} = (\rho, \rho u, \rho E)^\top$  is the vector of conservative variables,  $\mathbf{F} = (\rho u, \rho u^2 + p - \tau, \rho u E + pu - u\tau + q)^\top$  is the vector of fluxes,  $\mathbf{S} = (0, 0, \dot{Q})^\top$  is the vector of sources. Time is indicated with  $t$ ,  $x$  is the spatial coordinate,  $u$  is the velocity,  $\rho$  is the density,  $p$  is the thermodynamic pressure, and  $E = e + u^2/2$  is the specific, i.e., per unit mass, total energy (sum of specific internal energy and specific kinetic

energy). The Newtonian viscous stresses, expressed in accordance with Stokes's hypothesis, and the heat flux, modeled with Fourier heat conduction, are

$$\tau = \frac{4}{3}\mu \frac{\partial u}{\partial x}, \quad q = -k \frac{\partial T}{\partial x}, \tag{3}$$

where  $\mu$  is the dynamic viscosity,  $k$  is the thermal conductivity, and  $T$  is the absolute or thermodynamic temperature. Bulk viscosity effects were neglected due to the lack of available data in the literature for the fluids and flow conditions investigated in this work. The spatiotemporal distribution of the imposed volumetric heating rate  $\dot{Q}$  is given by

$$\dot{Q}(x, t) = \dot{\omega} g(x), \quad g(x) = \frac{1}{\ell\sqrt{2\pi}} e^{-\frac{1}{2}(x/\ell)^2}, \tag{4}$$

respectively, where  $\dot{\omega}$  (W/m<sup>2</sup>) is the planar heating rate and  $g(x)$  (m<sup>-1</sup>) is a Gaussian function with unitary (non-dimensional) integral on the real axis ( $\int_{-\infty}^{\infty} g(x)dx = 1$ ) with characteristic width  $\ell = 0.75$   $\mu$ m, inspired by the thin foil heater used in previous experiments [3]. Initial conditions are quiescent and uniform. For each initial condition, simulations are performed at several values of planar heating rate spanning five orders of magnitude, with upper bound limited by the occurrence of near-complete rarefaction of the fluid ( $\rho \rightarrow 0$ ) at the location of heat injection. The values of  $\dot{\omega}$  considered are  $10^5$ ,  $10^7$ ,  $10^9$ ,  $10^{10}$ ,  $3 \cdot 10^{10}$ , and  $6 \cdot 10^{10}$  W/m<sup>2</sup> for all initial conditions in Table 1 and  $10^{11}$ ,  $3 \cdot 10^{11}$ , and  $6 \cdot 10^{11}$  W/m<sup>2</sup> only for pseudo-liquid (PL) conditions. In total, 162 computations are analyzed in this study.

The computational setup (Fig. 3), which considers only  $x \geq 0$  with symmetry conditions imposed at  $x = 0$ , is sufficiently long to allow waves to form and track them numerically to determine their propagation Mach number,  $M$ . Simulations are halted before perturbations reach the right boundary of the computational domain (located at  $x = 20$   $\mu$ m). The analysis below focuses solely on the peak wave speed, measured upon coalescence of compression waves when and if shock formation occurs, but before the onset of wave amplitude decay due to thermoviscous losses. As such, the reported pressure jump values are independent from viscosity and conductivity.

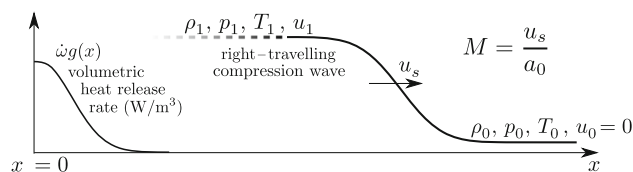


**Fig. 3** Computational setup for heat-induced wave generation. The post-compression state is denoted with the subscript 1, while pre-compression states are denoted with the subscript 0

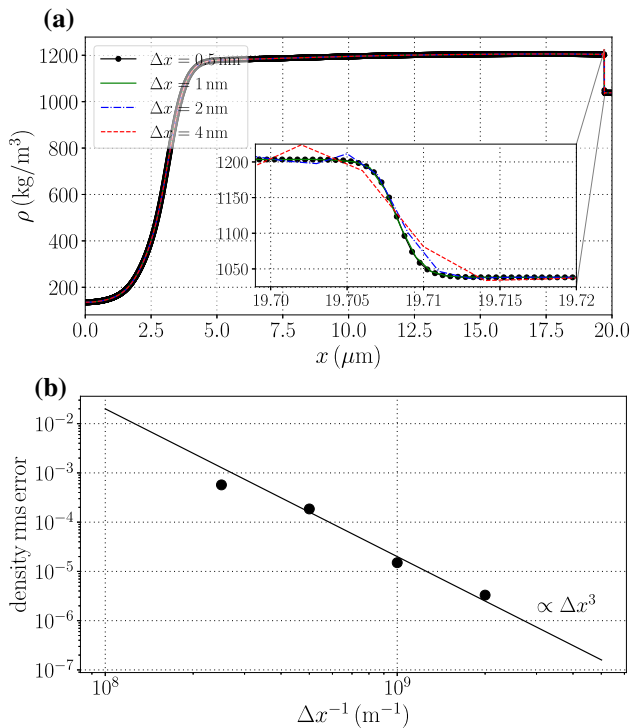


**Fig. 4** Grid convergence analysis for Navier–Stokes simulations of heat-induced shock waves in R-134a at PL conditions for  $\dot{\omega} = 6 \cdot 10^{10} \text{ W/m}^2$ . The grid selected for this case is the one with  $\Delta x = 0.5 \text{ nm}$ , and the reference solution employed for the convergence study is with  $\Delta x = 0.33 \text{ nm}$

Fully compressible Navier–Stokes simulations are performed with the solver *Hybrid* [41], which has extensively been used in the past for computations of shock waves. A fully conservative spatial discretization is employed to predict the correct shock speed [42], and a fourth-order Runge–Kutta scheme is employed for time advancement. The compression wave fronts are resolved with a minimum of 14 grid points (for the strongest shock) and with a time step of at most  $\Delta t = 0.01 \text{ ns}$ . A uniform grid was employed for all cases, ranging in grid spacing from  $\Delta x = 8 \text{ nm}$  (coarsest grid, used for weak shocks) to  $\Delta x = 0.5 \text{ nm}$  (finest grid, used for strong shocks). While the thus obtained shock profile, especially for the higher-Mach-number cases, is not physically accurate [43], this strategy avoids the adoption of shock-capturing schemes and still accurately predicts the jump of the thermo-fluid-dynamic quantities across the shock. Moreover, because of the numerical resolution employed, the results were not hindered by spurious pressure oscillations typically associated with transcritical flows [44,45], which are commonly contained by adopting dissipative and/or non-conservative schemes [46–48].

To assess the suitability of the grid resolution employed in this study, a grid convergence analysis has been performed on the most computationally demanding case (Fig. 4). Under-

resolved computations, yielding spurious oscillations around the shock location, are avoided by resolving with a sufficient amount of grid points all the computed shocks considered in this work (Fig. 4a). Away from the shock, the flow is well resolved even on the coarsest grids considered; furthermore, the numerical method is third-order accurate for this flow configuration (Fig. 4b). This analysis confirms that the flow-fields presented in this study are grid independent.

### 3 Results

#### 3.1 Linear regime

Combining the linearized mass and momentum equations, with the assumption of isentropic flow, yields

$$\frac{\partial^2}{\partial t^2} \delta p = a_0^2 \frac{\partial^2}{\partial x^2} \delta p, \tag{5}$$

where  $\delta p$  indicates a small pressure perturbation from the base state. The initial conditions for (5) are

$$(\delta p)_{t=0} = 0, \tag{6}$$

and

$$\left( \frac{\partial}{\partial t} \delta p \right)_{t=0} = \frac{\alpha_{p_0} a_0^2}{c_{p_0}} \dot{\omega} g(x), \tag{7}$$

where the latter is derived from the pressure evolution equation [49] evaluated at the initial time. With the initial conditions imposed by (6) and (7), d’Alembert’s analytical solution of (5) is given by

$$\frac{\delta p}{\rho_0 a_0^2} = \frac{\Omega}{2} \left[ \left( \frac{\sqrt{2} x + a_0 t}{2 \ell} \right) - \text{erf} \left( \frac{\sqrt{2} x - a_0 t}{2 \ell} \right) \right]. \tag{8}$$

The dimensionless linear pressure perturbation [left hand side of (8)] depends on the dimensionless space and time coordinates  $x/\ell$  and  $a_0 t/\ell$ , respectively, and on the dimensionless heating rate  $\Omega$ ; this normalization removes the dependence from the base state, and hence the specific fluid, achieving full collapse of the data as discussed below. The dimensionless heating rate is obtained by normalizing  $\dot{\omega}$  with the reference parameter plotted in Fig. 5, yielding

$$\Omega = \frac{\dot{\omega}}{2 \rho_0 a_0 c_{p_0} / \alpha_{p_0}} = \frac{G_0 \dot{\omega}}{2 \rho_0 a_0 \tilde{\gamma}_0}, \tag{9}$$

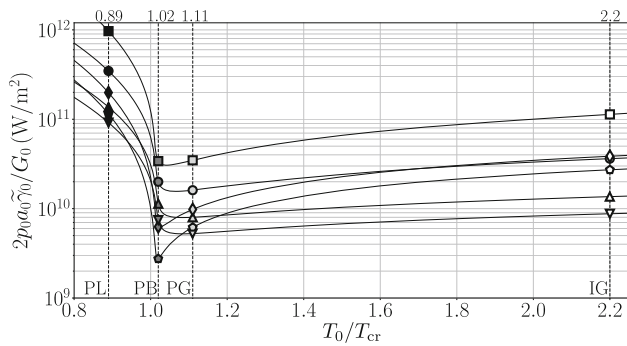


**Fig. 5** Reference scaling parameter for heating rate versus reduced temperature obtained through the PR EoS. The symbols correspond to the fluids and conditions in Table 1

where  $c_p$  is the isobaric specific thermal capacity, the Grüneisen parameter [50] is

$$G = \frac{\alpha_p a^2}{c_p} = \frac{\gamma - 1}{\alpha_p T}, \tag{10}$$

which reverts to  $\gamma - 1$  for ideal gases, where  $\gamma = c_{p0}/c_{v0}$  is the ratio of specific isobaric and isochoric thermal capacities, the relation  $a^2 T \alpha_p^2 / c_p = \gamma - 1$  has been used, and  $\tilde{\gamma}_0 = \rho_0 a_0^2 / p_0$  is the isentropic exponent [51]. We restrict the applicability of the present scaling strategy, and hence of the reference parameter used in (9), only to thermodynamic states with positive Grüneisen parameter  $G_0$ . The scaling does not apply, for example, to (near) isothermal acoustic waves (i.e.,  $\gamma_0$  tending to one) in dense gases or to fluids exhibiting non-standard Riemann problem solutions [52].

The dimensionless pressure jump across the compression wave,

$$\Pi = \frac{p_1 - p_0}{\rho_0 a_0^2}, \tag{11}$$

where the subscript 1 indicates the post-compression state (Fig. 3), is the classic definition of shock strength [53]. Comparing (8) and (11) yields

$$\Pi = \Omega. \tag{12}$$

This result is equivalent to the one obtained by Miura et al. [3], who predicted the amplitude of heat-induced linear acoustic waves via

$$p_1 - p_0 = \frac{\rho_0 a_0}{T_0} \left( \frac{\partial T}{\partial p} \right)_{s,0} \frac{\dot{\omega}}{2}, \tag{13}$$

which, using the thermodynamic relation  $(\partial T / \partial p)_s = \alpha_p T / (\rho c_p)$ , becomes

$$p_1 - p_0 = \frac{a_0 \alpha_p \rho_0}{c_p} \frac{\dot{\omega}}{2}, \tag{14}$$

which, made dimensionless with (9) and (11), reverts to (12).

Chu [27] used  $2\rho_0 a_0$  as the reference heating rate parameter for ideal gases. His scaling strategy, applied to the spatial pressure profiles considered in this study (Fig. 6a, b), does not collapse the data for all conditions considered in Table 1, not even among the IG cases. This is because Chu's scaling parameter does account for variations in  $\gamma$ , therefore collapsing only perfect ideal gases with the same value of  $\gamma$ . The IG cases considered in this work possess different values of  $\gamma$ , and thus, they can be properly scaled only if the reference heating rate is  $2\rho_0 c_{p0} a_0 T_0$  (Fig. 6c), equal to  $p_0 a_0 \gamma / (\gamma - 1)$  for perfect ideal gases. Still, this upgraded scaling parameter, which collapses well IG data, does not take into account real-fluid effects. This issue is resolved by replacing  $T_0$  with  $1/\alpha_{p0}$ , yielding full collapse of the numerical data across all fluids and conditions (Fig. 6d). For such low heating rates ( $\Omega \leq 3.634 \cdot 10^{-5}$ ), the compression waves satisfy the hyperbolic problem described by the linearized wave equation (5) and their dimensionless profiles all collapse into the functional law of (8). Notice that other scaling strategies not taking into account compressibility effects cannot achieve collapse of the data analyzed in this study (see Appendix 1).

The scaling parameters used in Fig. 6, whose data are limited to  $\Omega \leq 3.634 \cdot 10^{-5}$ , are also applied to the complete dataset (Figs. 7 and 8). Experimental data from Miura et al. [3] have also been included, using the provided dimensionless value of the density jump,  $\delta\rho/\rho_0 = 1.1 \cdot 10^{-7}$ , and the dimensional planar heating rate  $\dot{\omega} = 1830 \text{ W/m}^2$ . The dimensionless density jump is converted to a dimensionless pressure jump assuming isentropicity of the transformation ( $\delta\rho/\rho_0 = \delta p / (\rho_0 a_0^2)$ ), and the provided heating rate is made dimensionless via (9). Both numerical and experimental data are well collapsed (Fig. 7d) by the present scaling strategy [(9) and (11)] up to  $\Pi = 5.09$ . This result is not achieved by the other scaling strategies (Fig. 7b, c). Shock speeds extracted from the Navier–Stokes simulations (Fig. 9a) are also partially collapsed by following the proposed normalization of the heating rate (Fig. 9b). Moreover, even at the highest wave Mach number obtained, the flow inside the shock-wave thickness has been found to be in the continuum limit (see Appendix 2).

The scaling also allows to clearly observe (Figs. 8 and 9b) the departure from the linear prediction of (12), and to define linear ( $\Omega \leq 10^{-1}$ ) and nonlinear ( $\Omega \geq 10^{-1}$ ) regimes (Fig. 8). The dimensionless collapse obtained in the nonlinear regime suggests that an approximate prediction of the shock strength  $\Pi$  from the knowledge of the dimensionless heating rate  $\Omega$  only is possible. However, in the nonlinear regime, data follow a fluid- and state-specific departure from the linear prediction (see inset in Fig. 8), creating the need for a unified (linear and nonlinear) predictive modeling framework.

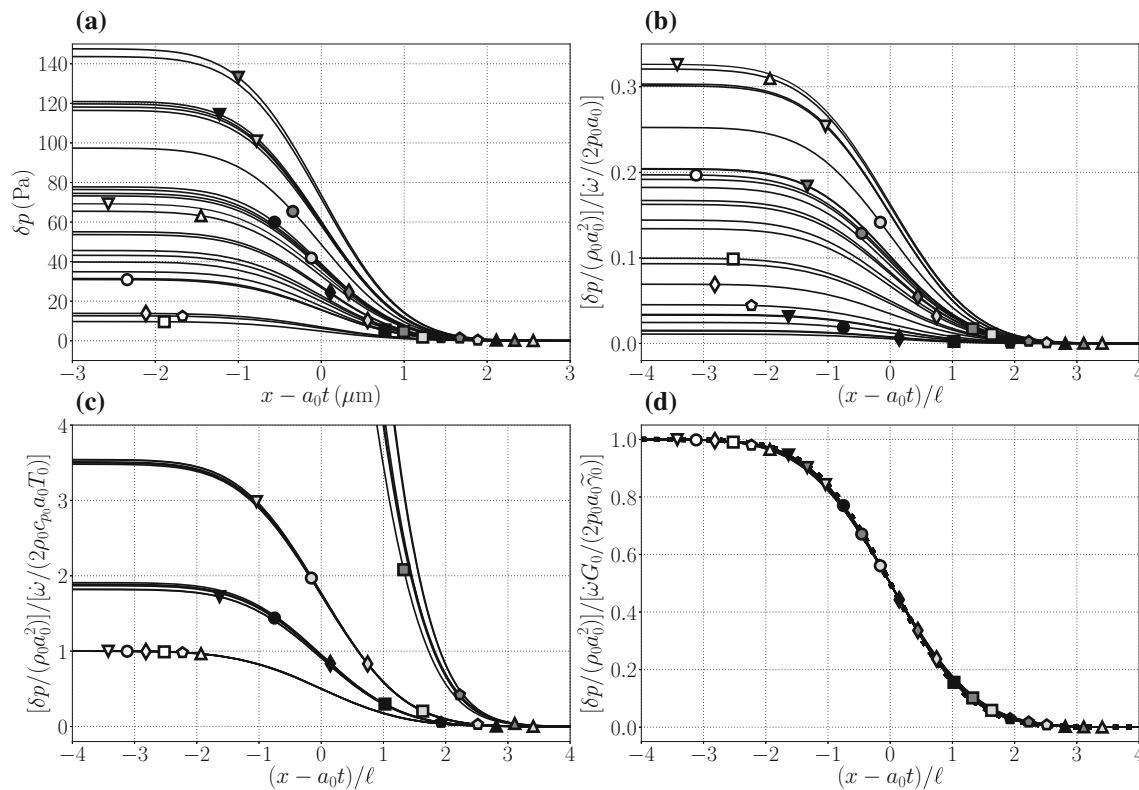


**Fig. 6** Scaling of linear pressure waveforms for heating rate  $\dot{\omega} = 10^5 \text{ W/m}^2$ . **a** Dimensional pressure profiles; **b** scaling proposed by Chu [27]; **c** scaling only collapsing IG data; **d** the proposed scaling (9, Fig. 5). The solution of the wave equation (8) is plotted as a thick dotted line in **d**. The maximum wave Mach number of the data shown

herein is  $M = 1.00003$ , and the dimensionless heating rate  $\Omega$  ranges from  $1.033 \cdot 10^{-7}$  to  $3.634 \cdot 10^{-5}$ , well within the linear regime (see Fig. 8). The symbols correspond to the fluids and conditions in Table 1 and are used here to distinguish the curves from one another

### 3.2 Nonlinear regime

We initially focus on the heat-induced flowfield in R-134a, shown in Fig. 10, as a representative case to guide our analysis and modeling of the nonlinear regime. The shocks, propagating to the right with speed  $u_s$ , are identifiable as sharp gradients in all thermo-fluid-dynamic quantities. By inspecting the dimensionless density variation profiles, what is identified as a smeared contact discontinuity (c.d.) is found moving approximately at the shock-induced Eulerian velocity  $u_1$ . Based on inviscid theory (Fig. 11a), across the c.d. pressure and velocity are continuous, but density and total energy jump from a steady post-shock state value to a zone at increasingly lower density, where heat is continuously supplied, referred to as the heated zone.

For a perfect ideal gas (IG, the first column of Fig. 10), the pressure and total energy in the post-shock and heated-zone regions are approximately uniform, and their values are set by the shock jump. In fact, IG pressure and volumetric internal energy are directly proportional via  $\rho e = p/(\gamma - 1)$ . This is one of the key assumptions made by Chu [27] in deriving

his predictive model for heat-induced waves in ideal gases, which is discussed later in (29).

For a supercritical fluid, instead, the relationship between pressure and volumetric internal energy is nonlinear and also dependent on another thermodynamic quantity such as temperature or density; hence, pressure and total energy perturbations exhibit real-fluid effects. Moreover, their spatial profiles between the shock wave and the heated-zone edge are not uniform. Finally, in the heated zone, total energy varies significantly with time and space, especially in PL conditions (the last column of Fig. 10), and pressure is not constant. All of the above reasonings set the stage for the modeling procedure outlined below.

The following analysis considers the mirrored extension of the semi-infinite problem in Fig. 3, from  $-\varepsilon$  to  $\varepsilon$ , where  $\varepsilon$  is an arbitrarily large number such that  $\varepsilon > u_s t$ . Inside this domain, the integral of the vector of conservative variables [see (2)] is

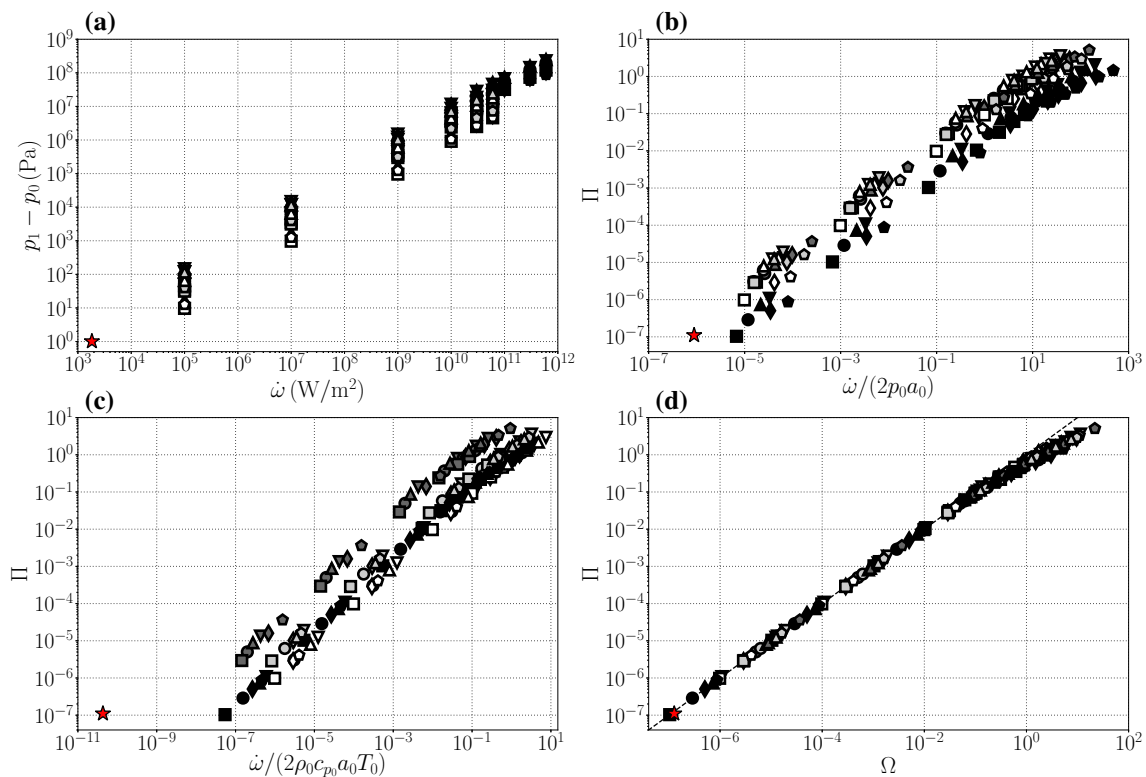


**Fig. 7** Scaling of pressure jumps obtained from the Navier–Stokes simulations versus heating rate. **a** Dimensional pressure jump  $\Pi$  versus dimensional heating rate  $\dot{\omega}$ ; **b** scaling proposed by Chu [27]; **c** alternative scaling collapsing only IG data; **d** the proposed scaling (9, Fig. 5). The prediction of (12) is shown with the dashed line in **d**. The star

at  $\Omega = 1.27 \cdot 10^{-7}$  and  $\Pi = 1.1 \cdot 10^{-7}$  represents the  $T_0 - T_{cr} = 150$  mK case by Miura et al. [3]. The other symbols correspond to pressure jumps for the fluids and conditions in Table 1. All data are included in supplementary material

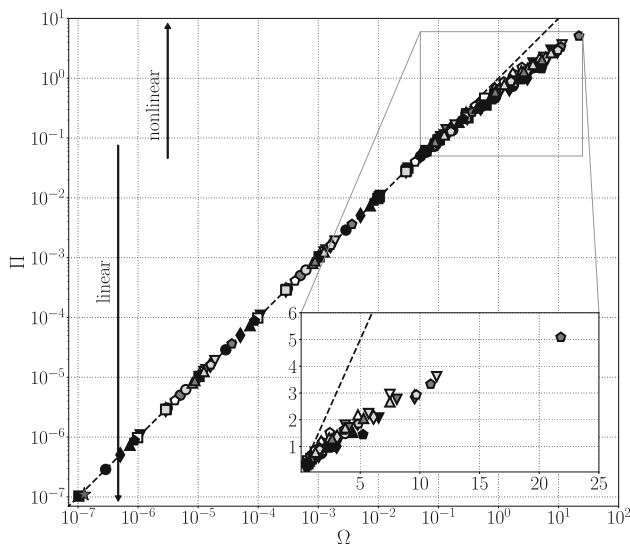


**Fig. 8** Shock strength  $\Pi$  versus dimensionless heating rates  $\Omega$ . Star:  $T_0 - T_{cr} = 150$  mK case by Miura et al. [3] with reported  $\Pi = 1.1 \cdot 10^{-7}$  and estimated  $\Omega = 1.27 \cdot 10^{-7}$ ; all other symbols: Navier–Stokes data for all combinations of conditions in Table 1. The linear prediction of (12) is shown with a dashed line. The highest shock strength is  $\Pi = 5.09$ , and the highest wave Mach number is  $M = 2.95$

$$\int_{-\varepsilon}^{\varepsilon} C(x, t) dx = \int_{-\varepsilon}^{-u_s t} C(x, t) dx + \int_{-u_s t}^{u_s t} C(x, t) dx + \int_{u_s t}^{\varepsilon} C(x, t) dx. \quad (15)$$

It should be noted that in the following derivation  $\varepsilon$  is not a function of time. In fact, a sufficiently large, fixed value of  $\varepsilon$  can always be found for a given time window of analysis,  $[0, t_f]$ , where  $t_f$  is picked sufficiently large to capture shock formation in all cases. The time variation of the left hand side of (15) is, after using Leibniz's rule for each term on its right hand side,

$$\frac{d}{dt} \int_{-\varepsilon}^{\varepsilon} C(x, t) dx = \int_{-\varepsilon}^{\varepsilon} \frac{\partial C(x, t)}{\partial t} dx, \quad (16)$$

which becomes, after exploiting the Navier–Stokes equations (2),

$$\frac{d}{dt} \int_{-\varepsilon}^{\varepsilon} C(x, t) dx = - \int_{-\varepsilon}^{\varepsilon} \frac{\partial F}{\partial x} dx + \int_{-\varepsilon}^{\varepsilon} S dx. \quad (17)$$

Using the definition of  $\dot{Q}$  in (4), and considering the flow

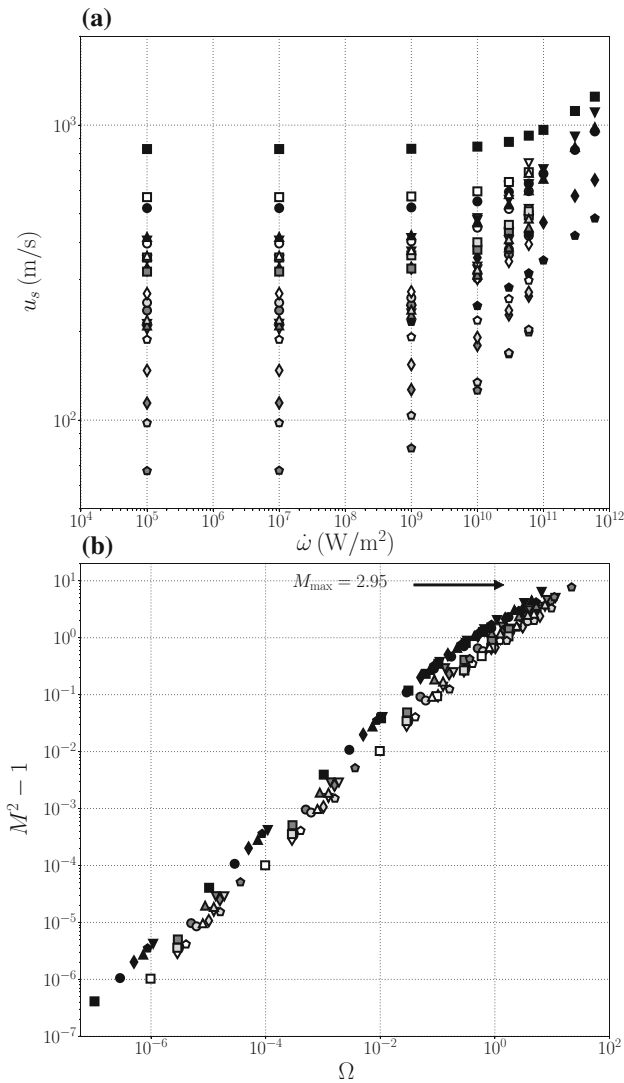


**Fig. 9** Scaling of shock speeds obtained from the Navier–Stokes simulations versus heating rates for all combinations of conditions reported in Table 1. **a** shock speed versus dimensional heating rate  $\dot{\omega}$ ; **b** Mach number squared minus unity versus dimensionless heating rate  $\Omega$

uniform and at rest for  $-\varepsilon \leq x < -u_s t$  and  $u_s t < x \leq \varepsilon$ , (17) becomes

$$\frac{d}{dt} \int_{-\varepsilon}^{\varepsilon} \mathbf{C}(x, t) dx = (0, 0, \dot{\omega})^T, \tag{18}$$

where  $\varepsilon$  is large enough so that  $\int_{-\varepsilon}^{\varepsilon} g(x) dx \simeq 1$ . Even if the heat input introduces a net integral of positive momentum in the  $x > 0$ -portion of the domain considered by the Navier–Stokes simulations, this analysis refers to the  $-\varepsilon < x < \varepsilon$  domain, for which the net change in the integral value of the momentum is zero, as stated in (18), due to symmetry of the problem about the  $x = 0$  location. Integrating (18) in time yields

$$\int_{-\varepsilon}^{\varepsilon} \mathbf{C}(x, t) dx - \int_{-\varepsilon}^{\varepsilon} \mathbf{C}(x, 0) dx = t(0, 0, \dot{\omega})^T, \tag{19}$$

which can be further manipulated to finally obtain

$$\int_{-u_s t}^{u_s t} \mathbf{C}(x, t) dx = t(2\rho_0 u_s, 0, 2\rho_0 e_0 u_s + \dot{\omega})^T. \tag{20}$$

If the profiles of  $\rho$  and  $\rho E$  are assumed to be symmetric with respect to the plane  $x = 0$ , (20) becomes

$$\begin{aligned} \frac{1}{t} \int_0^{u_s t} \rho dx &= \rho_0 u_s, \\ \frac{1}{t} \int_0^{u_s t} \rho E dx &= \rho_0 e_0 u_s + \frac{\dot{\omega}}{2}, \end{aligned} \tag{21}$$

and only  $x \geq 0$  is analyzed. For any given time, (21) can be written as

$$\int_0^M \rho d\xi = \rho_0 M, \quad \int_0^M \rho E d\xi = \rho_0 e_0 M + \frac{\dot{\omega}}{2a_0}, \tag{22}$$

where  $M = u_s/a_0$  is the wave Mach number and

$$\xi = \frac{x}{a_0 t}. \tag{23}$$

By inspecting Fig. 10, the idealized scenario illustrated in Fig. 11b is assumed, allowing to further develop (22), yielding

$$\rho_3 \mathcal{U} + \int_{\mathcal{U}}^M \rho_2 d\xi = \rho_0 M, \tag{24}$$

and

$$\rho_3 E_3 \mathcal{U} + \int_{\mathcal{U}}^M \rho_2 E_2 d\xi = \rho_0 e_0 M + \frac{\dot{\omega}}{2a_0}, \tag{25}$$

where  $\mathcal{U} = u_1/a_0$ . Only a suitable choice of  $\rho_2(\xi)$  in (24) and (25) is left for the prediction of heat-induced wave strength. We make the simplifying assumption of a linear functional form for  $\rho_2(\xi)$ ,

$$\rho_2(\xi) = \rho_3 + \frac{\xi - \mathcal{U}}{M - \mathcal{U}}(\rho_1 - \rho_3), \tag{26}$$

which inserted in (24) yields the value of the heated zone's density (Fig. 11b),

$$\rho_3 = \rho_1 \frac{M - \mathcal{U}}{M + \mathcal{U}}. \tag{27}$$

A different choice for the functional form of  $\rho_2(\xi)$  in (26) would change (27), but not the overall mass balance imposed by (24).

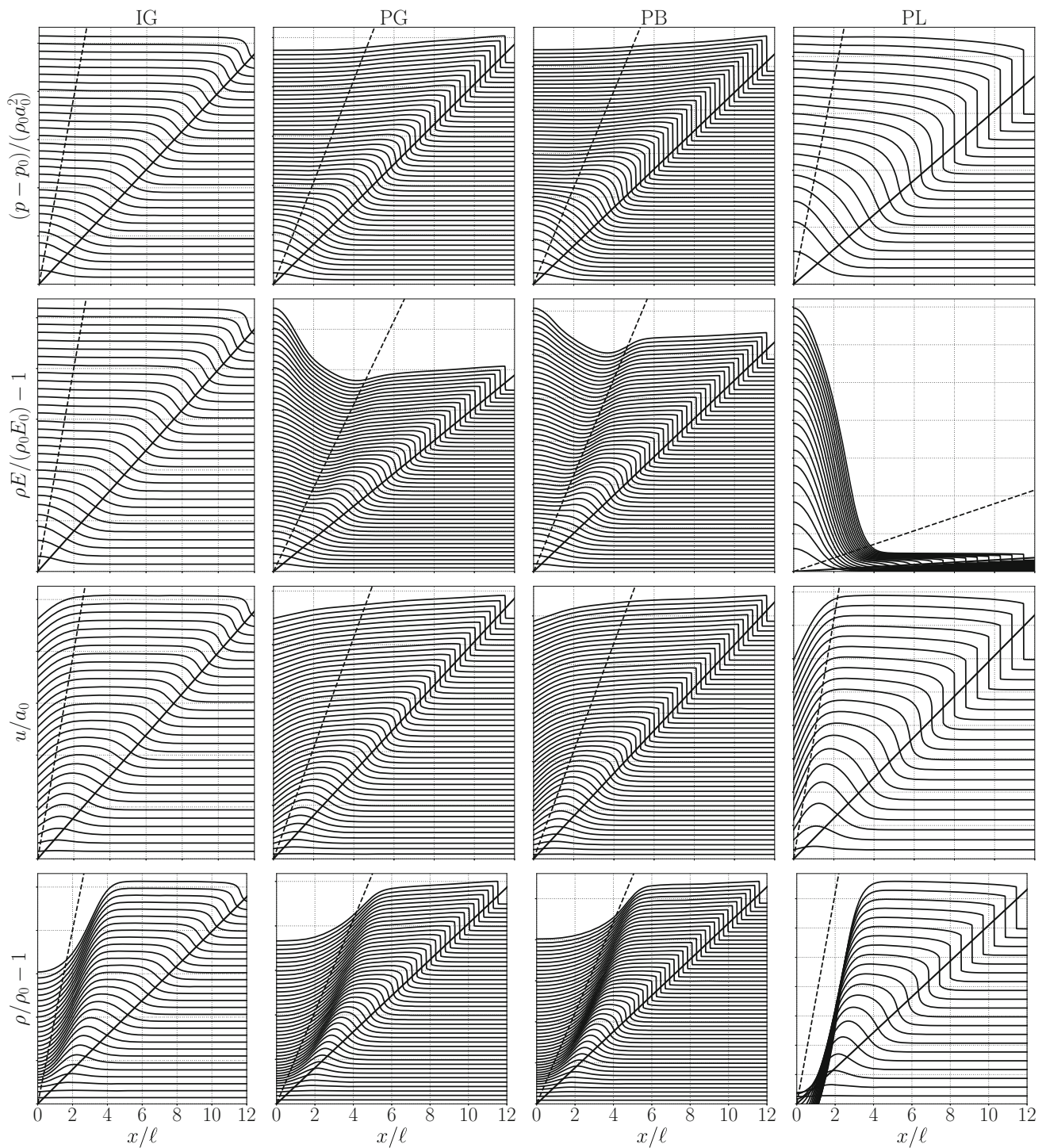
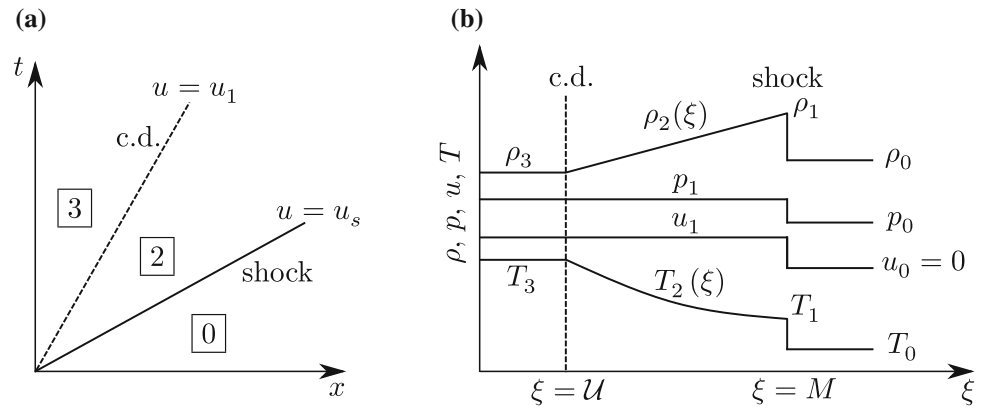


**Fig. 10** Rows: dimensionless perturbations of pressure, total energy, velocity, and density in R-134a, extracted from the Navier–Stokes simulations, plotted versus the dimensionless space coordinate  $x/\ell$  and shifted upward by an arbitrary value for every 1 ns of temporal evolution. Values of heat deposition rate for IG, PG, and PB:  $\dot{\omega} = 10^{10} \text{ W/m}^2$ ;

for PL:  $\dot{\omega} = 6 \cdot 10^{10} \text{ W/m}^2$ . Similar behavior is found for the other fluids and conditions (not shown). Solid oblique lines: maximum shock velocity ( $u = u_s$ ) obtained with a tracking algorithm; dashed oblique lines: heated-zone edge velocity (c.d.,  $u = u_1$ ) computed through the numerical solution of the RH equations with  $u_s$  as input

**Fig. 11** Schematics of heat-induced right-traveling shock wave and contact discontinuity (c.d.). **a** Shock and c.d. trajectory in the space–time plane; **b** assumed flow structure for heat-induced field in a supercritical fluid. The density profile  $\rho_2(\xi)$  is assumed to be linear (26), and the variable  $\xi$  is defined in (23)



In fact, the assumption  $\rho_2(\xi) = \rho_1$  made by Chu [27] allows, together with the first RH jump condition ( $\rho_1(u_s - u_1) = \rho_0 u_s$ ), to simplify (24) directly to

$$\rho_3 = 0. \tag{28}$$

Furthermore, when perfect ideal gases are considered,  $\rho_2 E_2 = p_1/(\gamma - 1) + \rho_1 u_1^2/2$  and the other RH equations simplify (25) to

$$p_1 u_1 = \frac{\gamma - 1}{2\gamma} \dot{\omega}, \tag{29}$$

which coincides with Eq. (34) of Chu’s article [27]. Given the uniform pressure of state 2,  $\rho_2 E_2$  is equal to its corresponding post-shock value,  $\rho_1 E_1$ , consistently with the flowfield observed in the IG column of Fig. 10. Equation (29) can be converted to the dimensionless form, yielding

$$\Omega = \frac{\sqrt{2}\Pi(\gamma\Pi + 1)}{\sqrt{\Pi(\gamma + 1) + 2}}, \tag{30}$$

which matches the parametrization derived in Eq. (39) of Chu’s paper [27], but recast following the normalization and symbology used in this paper [see (9) and (11)]. For  $\Pi \ll 1$ , (30) reverts to (12), removing the dependency from the ratio of specific heats  $\gamma$ . Equation (30) is only valid for perfect ideal gases, for which  $\rho_3 e_3$  is only a function of  $p_1$ .

Notice that  $\rho_3$  does not appear in (29); hence,  $\rho_3 = 0$  (28) is not relevant for the modeling of perfect ideal gases. However,  $\rho_3 = 0$  is non-physical for a real fluid and prevents the evaluation of the first term on the left hand side of (25), hence our different modeling assumption on the profile of  $\rho_2$  (26), which yields our assumed profile of  $\rho_3$  (27), which is not null. This modeling strategy is valid for supercritical fluids and can be used for perfect ideal gases as well, hence generalizing the model of Chu [27].

Equations (24) and (25) are solved with the following procedure, assuming all pre-shock values are known: first, for a given Mach number  $M$ , treated as input, the

Rankine–Hugoniot (RH) equations are solved numerically via a root finding algorithm, yielding all the post-shock quantities ( $\rho_1, p_1, u_1, T_1$ ); then,  $\rho_3$  is computed from (27), and  $e_3 = e(\rho_3, p_1)$  is obtained through the equation of state; finally, with the knowledge of  $\rho_2(\xi)$  (26),  $p_1$ , and  $u_1$ , the integral on the left hand side in (25) is computed, providing a value for  $\dot{\omega}$ . In summary, the result is the numerical determination of the following relation:

$$\dot{\omega} = \dot{\omega}(M, \rho_0, p_0, u_0), \tag{31}$$

where, for the particular setup considered here,  $u_0 = 0$ .

During the iterative procedure carried out on the RH equations, the admissibility problem of the non-unique solutions needs to be tackled. This is done by ensuring that Smith’s strong condition for uniqueness of the Riemann problem solution [52,54],  $\tilde{\gamma} > G$ , holds for all thermodynamic states considered. This corresponds to the medium condition of Menikoff et al. [52]. Furthermore, we also confirm that the fundamental derivative of gasdynamics [53] is positive (i.e., all isentropes are convex) for all cases considered in this work. Therefore, shock waves are of the compression type and yield a positive entropy jump.

The proposed model for heat-induced waves accurately predicts the fluid- and state-specific trends exhibited by data extracted from the Navier–Stokes simulations (Fig. 12), for all initial conditions in Table 1. In the nonlinear regime, the ratio of the dimensionless pressure jump to the dimensionless heating rate,  $\Pi/\Omega$ , is maximum for perfect ideal gases and minimum for fluids in pseudo-liquid conditions (Fig. 12) and is, in all cases, always upper-bounded by the linear prediction  $\Pi/\Omega = 1$ .

The information gathered from the plots of the ratio  $\Pi/\Omega$  is not sufficient to establish a quantitative measure for the efficiency of thermal to mechanical power conversion, which is instead given in the next section.

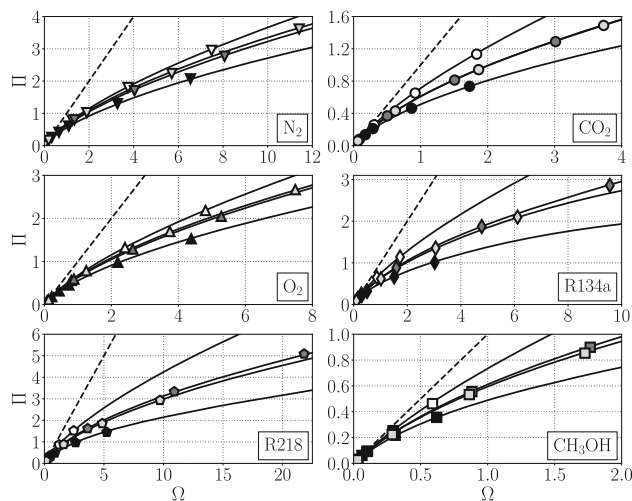


**Fig. 12** Fluid-by-fluid shock strength versus dimensionless heating rate showing deviation from the prediction of (12) (dashed line): Navier–Stokes simulations corresponding to the fluids and conditions in Table 1 (symbols) and results from the modeling strategy ((24) and (25), solid lines). IG data (white-filled symbols) lay on the curve defined by 30. The linear scale in this figure hides data from the low-amplitude linear compression wave cases (compare with Fig. 8)

### 3.3 Efficiency of thermal to mechanical power conversion

A quantitative metric for the efficiency of thermal to mechanical power conversion can be obtained by dividing the mechanical power carried by the shocks,  $2(p_1 - p_0)u_1$ , by the total heat power input,  $\dot{\omega}$ ,

$$\eta = \frac{(p_1 - p_0)u_1}{\dot{\omega}/2}. \tag{32}$$

(32) can be recast in the dimensionless form, after using the Rankine–Hugoniot equations, yielding

$$\eta = G_0 \frac{\Pi^2}{\Omega M}, \tag{33}$$

where  $G_0$  is the base Grüneisen parameter (10), which is used, in the context of thermoacoustic energy conversion [55], as the ratio between the work parameter  $\gamma - 1$  and the heat parameter  $\alpha_p T$ .

The efficiency computed from the Navier–Stokes data is accurately predicted by the model outlined in Sect. 3.2, as shown in Fig. 13. For linear waves, the efficiency in (33) is approximately given by

$$\eta = G_0 \Pi \tag{34}$$

and is the highest for fluids in PL conditions, followed by PB, PG, and then IG conditions. On the other hand, as the dimensionless heating rate increases and the waves become

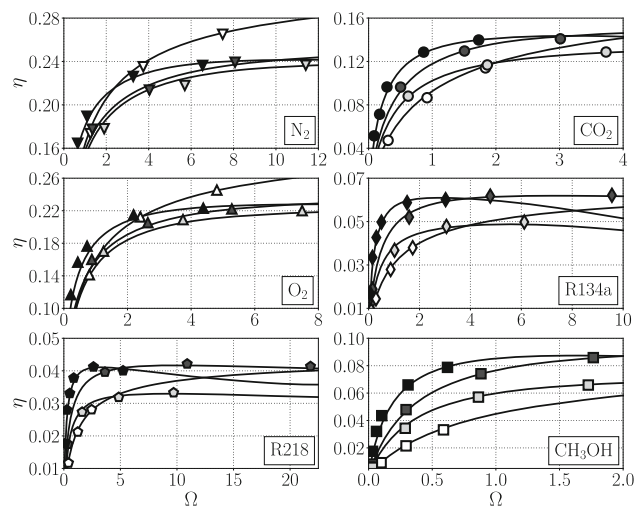


**Fig. 13** Fluid-by-fluid shock thermal to mechanical energy conversion efficiency (32) versus dimensionless heating rate  $\Omega$ : Navier–Stokes simulations corresponding to the fluids and conditions in Table 1 (symbols) and results from the modeling strategy (24 and 25, solid lines)

nonlinear, the efficiency of perfect ideal gases grows, until it becomes the highest among all fluid conditions considered. The highest efficiencies are achieved in  $N_2$  and  $O_2$ , the lowest in R134a and R218, with  $CO_2$  and methanol in between, indicating that heavier fluids convert heat into mechanical work more poorly.

In the limit of  $\Omega \rightarrow \infty$ , both the perfect ideal gas EoS and the PR EoS cease to be physically representative of the existing fluids. Nonetheless, it is of theoretical interest to investigate the asymptotic behavior of heat-induced waves in supercritical fluids, as done by Chu [27] for ideal gases.

For  $\Omega \gg 1$  and, thus, shock strength  $\Pi \gg 1$ , (30), valid for a perfect ideal gas, reverts to the two-thirds law proposed in Eq. (40) by Chu [27], which can be recast as

$$\Pi = \left(\frac{\gamma + 1}{2}\right)^{1/3} \left(\frac{\Omega}{\gamma}\right)^{2/3}. \tag{35}$$

Thus, fluids in IG conditions tend to an asymptotic thermal to mechanical power conversion efficiency,

$$\eta = 1 - \frac{1}{\gamma}, \tag{36}$$

where we used the RH equations, (35), and (33).

For supercritical fluids, instead, the ratio  $\Pi/\Omega$  tends to values lower than the ones obtained with fluids in IG conditions (Fig. 14a), and the efficiency  $\eta$  eventually decreases to values even inferior to the ones of the linear regime (Fig. 14b). The asymptotic behavior shown in Fig. 14 concerns the jumps across the shocks, which rapidly abandon the heated region due to their supersonic propagation speed.

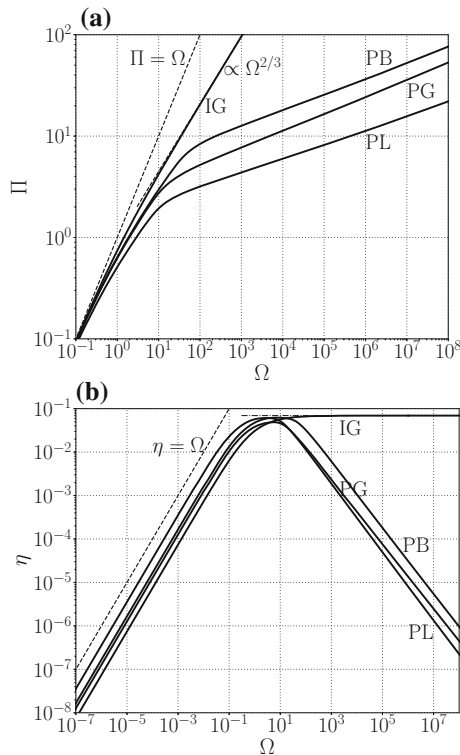


**Fig. 14** Results from the predictive model (24 and 25) for R-134a in different thermodynamic states. **a** Shock strength  $\Pi$  versus dimensionless heating rate  $\Omega$ ; **b** efficiency of thermal to mechanical power conversion  $\eta$  (32) versus  $\Omega$ . Equations (12) and (35) are plotted with a dashed line in **a**, and (36) is plotted with a dashed-dotted line in **b**

Hence, there should be no practical or theoretical expectation of  $\Omega \rightarrow \infty$  representing an ideal gas case for the shock dynamics per se. This can be further explained, keeping (25) in mind, by observing the profiles in Fig. 10, imagined in the limit of  $\Omega \gg 1$ . For IG conditions, the heated zone's total energy does not increase significantly in time, regardless of the imposed heating rate, implying that all of the injected power directly sustains shock-wave propagation. On the other hand, for real fluids, the nonlinear relationships between thermodynamic variables entail a significant change of volumetric internal energy, even with the slight variations of pressure present in the heated zone. For PL conditions, in particular, most of the injected power is retained by the heated zone, allowing less power to flow toward the shock wave.

## 4 Conclusions

In summary, we have investigated heat-induced planar compression waves, generated by a Gaussian-shaped source term in the total energy equation, in six different fluids at

supercritical pressure and in pseudo-liquid, pseudo-boiling, pseudo-gaseous, and ideal-gas conditions.

The reference heating rate parameter, expressed appropriately in terms of the base isobaric thermal expansion coefficient, collapses data from one-dimensional Navier–Stokes numerical simulations and from experimental results of Miura et al. [3]. The scaling strategy also outlines the division between linear and nonlinear regimes.

The real-fluid effects on the structure of the nonlinear flow-field have been revealed, and a fully predictive model, based on global mass and energy conservation, has been proposed, generalizing the results of Chu [27] to supercritical fluids.

Finally, the thermal to mechanical power conversion efficiency in the linear regime has been shown to be proportional to the base Grüneisen parameter, which is maximum for fluids in pseudo-liquid conditions. However, the efficiency in the nonlinear regime is eventually the highest in ideal gases. In supercritical fluids, in fact, the nonlinear energy pathways inside the heated zone lead to a thermodynamic bottleneck for energy conversion.

Future challenges for this work lie in addressing two-dimensional and three-dimensional effects, including and/or obtaining bulk viscosity data for each fluid at various shock amplitudes, and derive appropriate thermodynamic closures when and if flow conditions entail loss of equilibrium at a molecular scale.

**Acknowledgements** MTM acknowledges the support of the Frederick N. Andrews and Rolls-Royce Doctoral Fellowships from Purdue University. The authors thank Pat Sweeney (Rolls-Royce) and Stephen D. Heister (Purdue) for the fruitful discussions that have inspired the need for scaling across different fluids. The computing resources were provided by the Rosen Center for Advanced Computing (RCAC) at Purdue University and Information Technology at Purdue (ITaP). The authors finally thank the two anonymous reviewers and the editor for their very useful comments during the review process.

## Appendix 1: Application of the Widom-line similarity law

The post-shock states, indicated with a subscript 1, obtained in this work span the ranges  $p_1/p_{cr} = 1.1 - 69$  and  $T_1/T_{cr} = 0.89 - 4.34$  (Fig. 15a), covering a large portion of the supercritical state space. As expected, fluids in PL conditions tend to exhibit the largest pressure response to small heat-induced temperature changes, while fluids in IG conditions exhibit the weakest response. The dataset, if scaled using the recently proposed similarity law for Widom lines [56] (Fig. 15b), does not show collapse onto a fluid-independent curve for each initial condition (see Table 1). The Widom-line similarity proposed in [56], which was derived focusing on the  $p/p_{cr} < 3$  region, is able to only partially scale some of the data for PG fluids (see inset of Fig. 15b); overall, it

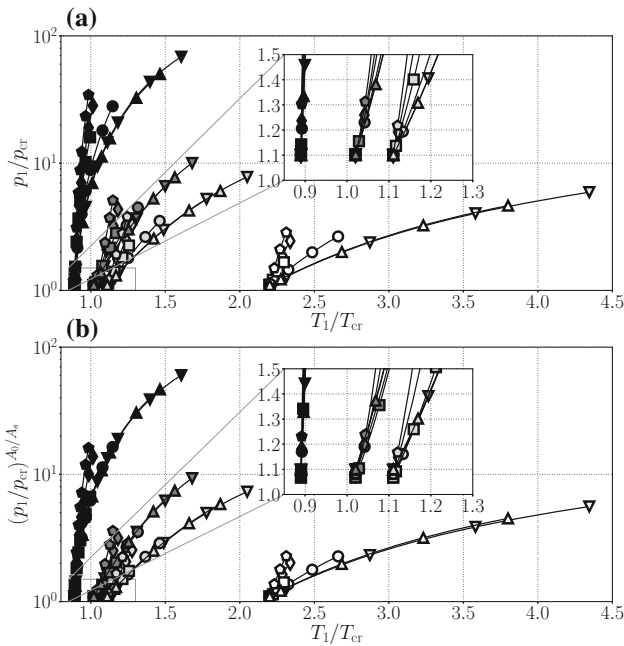


**Fig. 15** Post-shock thermodynamic states plotted in the reduced pressure versus reduced temperature space (a) and in the scaled reduced pressure [56] versus reduced temperature space (b).  $A_0 = 5.52$  for all fluids, while  $A_s = 6.57$  for  $\text{CO}_2$ ,  $A_s = 5.63$  for  $\text{O}_2$ ,  $A_s = 5.7$  for  $\text{N}_2$ ,  $A_s = 7.02$  for R-218,  $A_s = 7.03$  for R-134a, and  $A_s = 8.06$  for  $\text{CH}_3\text{OH}$ . Solid lines and symbols (see Table 1) correspond to the numerical solution of the Rankine–Hugoniot equations

lacks the ability to successfully scale data from simulations of acoustic and shock waves.

## Appendix 2: Knudsen number analysis

Supercritical fluids undergoing pseudo-phase change are characterized by a molecular reorganization process [34,57] with an associated finite timescale. This raises concerns regarding excessively thin shocks, yielding short fluid particle residence times, challenging the validity of the thermodynamic equilibrium assumption implicit in the present calculations.

In this study, the predicted particle residence times in the shock range from  $4.7 \cdot 10^{-3}$  ns to 0.8 ns, with fluids in PL conditions yielding the shortest residence times. Due to the lack of data on molecular relaxation times for all of the fluids analyzed here, we revert to an analysis based on the Knudsen number to establish the likelihood of loss of equilibrium in the shocks considered. An excessively high Kn number, approaching the rarefied regime, would imply a low number of collisions for a given shock thickness, hence longer relaxation times. The relevant Knudsen number in this case is

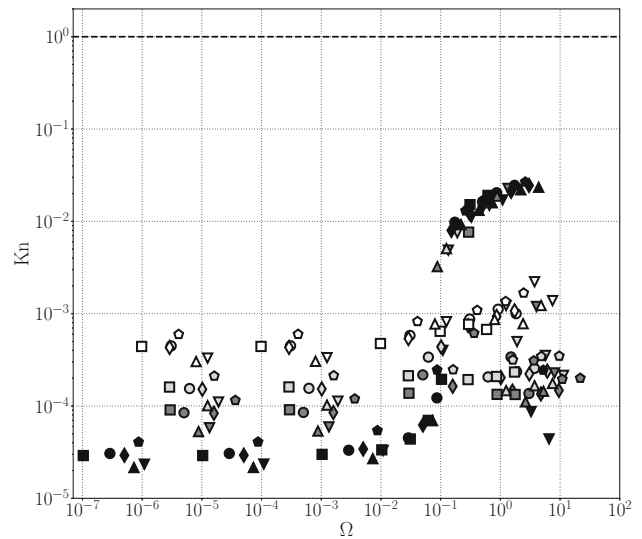


**Fig. 16** Knudsen numbers for the heat-induced shocks computed through Navier–Stokes simulations for the fluids and conditions in Table 1

$$\text{Kn} = \frac{\lambda}{\delta_s}, \tag{37}$$

where  $\delta_s$  is the shock thickness, as measured from the Navier–Stokes simulations, and an order-of-magnitude approximate estimate for the mean free path [58]  $\lambda$  is

$$\lambda = \frac{M_m}{\sqrt{2\pi}d^2\rho_0N_A}, \tag{38}$$

where  $N_A = 6.02214076 \cdot 10^{23}$  1/mol is the Avogadro number,  $M_m$  is the molar mass, and  $d$  is the molecular kinetic diameter, which is  $d = 0.33$  nm for  $\text{CO}_2$ ;  $d = 0.364$  nm for  $\text{N}_2$ ;  $d = 0.346$  nm for  $\text{O}_2$  [59];  $d = 0.41$  nm for methanol ( $\text{CH}_3\text{OH}$ ) [60]; and  $d = 0.5$  nm for R-134a and R-218 (estimated from data of [61] on similar molecules).

The shock thicknesses extracted from the simulations  $\delta_s$  range from 4.6 nm to 5.4  $\mu\text{m}$ , with the important caveat that fully resolved shock profiles from Navier–Stokes simulations are only physically relevant for Mach numbers sufficiently close to unity [43] and, moreover, that the values of  $\delta_s$  stem from a thermodynamic equilibrium assumption. The maximum wave Mach number observed in this study is 2.95 (see Fig. 9b). As such, the values of  $\delta_s$  used here serve as estimates, which are expected to be sufficiently accurate for this analysis as the details of the inner shock profile depend on the choice of the EoS and the transport quantities which do account for real-fluid effects.

As apparent from the data shown in Fig. 16, the vast majority of the shocks are well within the continuum regime ( $\text{Kn} \ll 1$ ), primarily due to the high base pressures and densities. We hence conclude that a fluid parcel undergoing compression across the shock is experiencing enough

collisions at a molecular level to stay in thermodynamic equilibrium. The highest values of  $Kn$ , of around 0.03, are achieved by fluids in PL conditions for dimensionless heat deposition rates of  $\Omega > 0.1$  and pose the most significant challenge to the assumption of thermodynamic equilibrium.

## References

- Kassoy, D.R.: The response of a confined gas to a thermal disturbance. I: Slow transients. *SIAM J. Appl. Math.* **36**(3), 624–634 (1979). <https://doi.org/10.1137/0136044>
- Sutrisno, I., Kassoy, D.R.: Weak shocks initiated by power deposition on a spherical source boundary. *SIAM J. Appl. Math.* **51**(3), 658–672 (1991). <https://doi.org/10.1137/0151033>
- Miura, Y., Yoshihara, S., Ohnishi, M., Honda, K., Matsumoto, M., Kawai, J., Ishikawa, M., Kobayashi, H., Onuki, A.: High-speed observation of the piston effect near the gas–liquid critical point. *Phys. Rev. E* **74**, 010101 (2006). <https://doi.org/10.1103/PhysRevE.74.010101>
- Clarke, J.F., Kassoy, D.R., Riley, N.: Shocks generated in a confined gas due to rapid heat addition at the boundary. II. Strong shock waves. *Proc. R. Soc. Lond. A* **393**(1805), 331–351 (1984). <https://doi.org/10.1098/rspa.1984.0061>
- Boslough, M., Crawford, D.: Low-altitude airbursts and the impact threat. *Int. J. Impact Eng.* **35**(12), 1441–1448 (2008). <https://doi.org/10.1016/j.ijimpeng.2008.07.053>
- National Research Council: *Defending Planet Earth: Near-Earth-Object Surveys and Hazard Mitigation Strategies*. The National Academies Press, Washington, D.C. (2010). <https://doi.org/10.17226/12842>
- Taylor, G.: The formation of a blast wave by a very intense explosion. I. Theoretical discussion. *Proc. R. Soc. Lond. A: Math. Phys. Eng. Sci.* **201**(1065), 159–174 (1950). <https://doi.org/10.1098/rspa.1950.0049>
- Suk, J.W., Kirk, K., Hao, Y., Hall, N.A., Ruoff, R.S.: Thermoacoustic sound generation from monolayer graphene for transparent and flexible sound sources. *Adv. Mater.* **24**(47), 6342–6347 (2012). <https://doi.org/10.1002/adma.201201782>
- Liu, Q., Zhang, Y.: Shock wave generated by high-energy electric spark discharge. *J. Appl. Phys.* **116**(15), 153302 (2014). <https://doi.org/10.1063/1.4898141>
- Temkin, S.: A model for thunder based on heat addition. *J. Sound Vib.* **52**(3), 401–414 (1977). [https://doi.org/10.1016/0022-460X\(77\)90567-3](https://doi.org/10.1016/0022-460X(77)90567-3)
- Krane, R.J., Parang, M.: Scaling analysis of thermoacoustic convection in a zero-gravity environment. *J. Spacecr. Rockets* **20**(3), 316–317 (1983). <https://doi.org/10.2514/3.25598>
- Carlès, P.: Thermoacoustic waves near the liquid–vapor critical point. *Phys. Fluids* **18**(12), 126102 (2006). <https://doi.org/10.1063/1.2397577>
- Shen, B., Zhang, P.: Thermoacoustic waves along the critical isochore. *Phys. Rev. E* **83**, 011115 (2011). <https://doi.org/10.1103/PhysRevE.83.011115>
- Onuki, A., Hao, H., Ferrell, R.A.: Fast adiabatic equilibration in a single-component fluid near the liquid–vapor critical point. *Phys. Rev. A* **41**, 2256–2259 (1990). <https://doi.org/10.1103/PhysRevA.41.2256>
- Boukari, H., Briggs, M.E., Shaumeyer, J.N., Gammon, R.W.: Critical speeding up observed. *Phys. Rev. Lett.* **65**, 2654–2657 (1990). <https://doi.org/10.1103/PhysRevLett.65.2654>
- Zappoli, B., Bailly, D., Garrabos, Y., Le Neindre, B., Guenoun, P., Beysens, D.: Anomalous heat transport by the piston effect in supercritical fluids under zero gravity. *Phys. Rev. A* **41**, 2264–2267 (1990). <https://doi.org/10.1103/PhysRevA.41.2264>
- Amiroudine, S., Zappoli, B.: Piston-effect-induced thermal oscillations at the Rayleigh–Bénard threshold in supercritical  $^3\text{He}$ . *Phys. Rev. Lett.* **90**, 105303 (2003). <https://doi.org/10.1103/PhysRevLett.90.105303>
- Zappoli, B.: Near-critical fluid hydrodynamics. *Comptes Rendus Mécanique* **331**(10), 713–726 (2003). <https://doi.org/10.1016/j.crme.2003.05.001>
- Onuki, A.: Thermoacoustic effects in supercritical fluids near the critical point: resonance, piston effect, and acoustic emission and reflection. *Phys. Rev. E* **76**, 061126 (2007). <https://doi.org/10.1103/PhysRevE.76.061126>
- Carlès, P.: A brief review of the thermophysical properties of supercritical fluids. *J. Supercrit. Fluids* **53**(1–32), 2–11 (2010). <https://doi.org/10.1016/j.supflu.2010.02.017>
- Brown, M.A., Churchill, S.W.: Experimental measurements of pressure waves generated by impulsive heating of a surface. *AIChE J.* **41**(2), 205–213 (1995). <https://doi.org/10.1002/aic.690410202>
- Zappoli, B., Durand-Daubin, A.: Direct numerical modelling of heat and mass transport in a near supercritical fluid. *Acta Astronaut.* **29**(10/11), 847–859 (1993). [https://doi.org/10.1016/0094-5765\(93\)90167-U](https://doi.org/10.1016/0094-5765(93)90167-U)
- Nakano, A.: Studies on piston and soot effects in a binary mixture supercritical fluid. *Int. J. Heat Mass Transf.* **50**(23–24), 4678–4687 (2007). <https://doi.org/10.1016/j.ijheatmasstransfer.2007.03.014>
- Hasan, N., Farouk, B.: Thermoacoustic transport in supercritical fluids at near-critical and near-pseudo-critical states. *J. Supercrit. Fluids* **68**, 13–24 (2012). <https://doi.org/10.1016/j.supflu.2012.04.007>
- Hwang, I.J., Kim, Y.J.: Measurement of thermo-acoustic waves induced by rapid heating of nickel sheet in open and confined spaces. *Int. J. Heat Mass Transf.* **49**(3–4), 575–581 (2006). <https://doi.org/10.1016/j.ijheatmasstransfer.2005.08.025>
- Hasan, N., Farouk, B.: Fast heating induced thermoacoustic waves in supercritical fluids: experimental and numerical studies. *J. Heat Transf.* **135**(8), 081701 (2013). <https://doi.org/10.1115/1.4024066>
- Chu, B.T.: Pressure waves generated by addition of heat in a gaseous medium. NASA Technical Report, NACA-TN 3411 (1955). <https://ntrs.nasa.gov/search.jsp?R=19930084155>
- Argrow, B.M.: Computational analysis of dense gas shock tube flow. *Shock Waves* **6**(4), 241–248 (1996). <https://doi.org/10.1007/BF02511381>
- Schlamp, S., Rösgen, T.: Flow in near-critical fluids induced by shock and expansion waves. *Shock Waves* **14**(1), 93–101 (2005). <https://doi.org/10.1007/s00193-004-0241-6>
- Mortimer, B., Skews, B., Felthun, L.: The use of a slow sound speed fluorocarbon liquid for shock wave research. *Shock Waves* **8**(2), 63–69 (1998). <https://doi.org/10.1007/s001930050099>
- Kim, H., Choe, Y., Kim, H., Min, D., Kim, C.: Methods for compressible multiphase flows and their applications. *Shock Waves* **29**(1), 235–261 (2019). <https://doi.org/10.1007/s00193-018-0829-x>
- Re, B., Guardone, A.: An adaptive ALE scheme for non-ideal compressible fluid dynamics over dynamic unstructured meshes. *Shock Waves* **29**(1), 73–99 (2019). <https://doi.org/10.1007/s00193-018-0840-2>
- Fisher, M.E., Widom, B.: Decay of correlations in linear systems. *J. Chem. Phys.* **50**(20), 3756–3772 (1969). <https://doi.org/10.1063/1.1671624>
- Tucker, S.C.: Solvent density inhomogeneities in supercritical fluids. *Chem. Rev.* **99**(2), 391–418 (1999). <https://doi.org/10.1021/cr9700437>
- Banuti, D.T.: Crossing the widom-line—supercritical pseudo-boiling. *J. Supercrit. Fluids* **98**, 12–16 (2015). <https://doi.org/10.1016/j.supflu.2014.12.019>

36. Lemmon, E.W., McLinden, M.O., Friend, D.G.: Thermophysical Properties of Fluid Systems in NIST Chemistry WebBook, NIST Standard Reference Database Number 69. National Institute of Standards and Technology, Gaithersburg MD, 20899 (2019). <https://doi.org/10.18434/T4D303>
37. Poling, B.E., Prausnitz, J.M., O'Connell, J.P.: The Properties of Gases and Liquids, 5th edn. McGraw-Hill Education, New York (2001)
38. Peng, D.Y., Robinson, D.B.: A new two-constant equation of state. *Ind. Eng. Chem. Fundam.* **15**(1), 59–64 (1976). <https://doi.org/10.1021/i160057a011>
39. Chung, T.H., Ajlan, M., Lee, L.L., Starling, K.E.: Generalized multiparameter correlation for nonpolar and polar fluid transport properties. *Ind. Eng. Chem. Res.* **27**(4), 671–679 (1988). <https://doi.org/10.1021/ie00076a024>
40. Kim, K., Hickey, J.P., Scalo, C.: Pseudophase change effects in turbulent channel flow under transcritical temperature conditions. *J. Fluid Mech.* **871**, 52–91 (2019). <https://doi.org/10.1017/jfm.2019.292>
41. Larsson, J., Lele, S.K.: Direct numerical simulation of canonical shock/turbulence interaction. *Phys. Fluids* **21**(12), 126101 (2009). <https://doi.org/10.1063/1.3275856>
42. Toro, E.F.: Anomalies of conservative methods: analysis, numerical evidence and possible cures. *Comput. Fluids Dyn. J.* **11**(2), 128–143 (2002)
43. Bird, G.A.: *Molecular Gas Dynamics and the Direct Simulation of Gas Flows*. Oxford University Press, Oxford (1994)
44. Karni, S.: Multicomponent flow calculations by a consistent primitive algorithm. *J. Comput. Phys.* **112**(1), 31–43 (1994). <https://doi.org/10.1006/jcph.1994.1080>
45. Abgrall, R.: How to prevent pressure oscillations in multicomponent flow calculations: a quasi conservative approach. *J. Comput. Phys.* **125**(1), 150–160 (1996). <https://doi.org/10.1006/jcph.1996.0085>
46. Kawai, S., Terashima, H., Negishi, H.: A robust and accurate numerical method for transcritical turbulent flows at supercritical pressure with an arbitrary equation of state. *J. Comput. Phys.* **300**(Supplement C), 116–135 (2015). <https://doi.org/10.1016/j.jcp.2015.07.047>
47. Ma, P.C., Lv, Y., Ihme, M.: An entropy-stable hybrid scheme for simulations of transcritical real-fluid flows. *J. Comput. Phys.* **340**(Supplement C), 330–357 (2017). <https://doi.org/10.1016/j.jcp.2017.03.022>
48. Migliorino, M.T., Chapelier, J.B., Scalo, C., Lodato, G.: Assessment of spurious numerical oscillations in high-order spectral difference solvers for supercritical flows. 2018 Fluid Dynamics Conference, AIAA Aviation Forum, AIAA Paper 2018-4273 (2018). <https://doi.org/10.2514/6.2018-4273>
49. Migliorino, M.T., Scalo, C.: Dimensionless scaling of heat-release-induced planar shock waves in near-critical CO<sub>2</sub>. 55th Aerospace Sciences Meeting, AIAA SciTech Forum, AIAA Paper 2017-0086 (2017). <https://doi.org/10.2514/6.2017-0086>
50. Grüneisen, E.: Theorie des festen Zustandes einatomiger Elemente. *Ann. Phys.* **344**(12), 257–306 (1912). <https://doi.org/10.1002/andp.19123441202>
51. Iberall, A.S.: The effective “Gamma” for isentropic expansions of real gases. *J. Appl. Phys.* **19**(11), 997–999 (1948). <https://doi.org/10.1063/1.1698089>
52. Menikoff, R., Plohr, B.J.: The Riemann problem for fluid flow of real materials. *Rev. Mod. Phys.* **61**, 75–130 (1989). <https://doi.org/10.1103/RevModPhys.61.75>
53. Thompson, P.A.: A fundamental derivative in gasdynamics. *Phys. Fluids* **14**(9), 1843–1849 (1971). <https://doi.org/10.1063/1.1693693>
54. Smith, R.G.: The Riemann problem in gas dynamics. *Trans. Am. Math. Soc.* **249**(1), 1–50 (1979). <https://doi.org/10.1090/S0002-9947-1979-0526309-2>
55. Swift, G.W., Migliori, A., Hofer, T., Wheatley, J.: Theory and calculations for an intrinsically irreversible acoustic prime mover using liquid sodium as primary working fluid. *J. Acoust. Soc. Am.* **78**(2), 767–781 (1985). <https://doi.org/10.1121/1.392447>
56. Banuti, D.T., Raju, M., Ihme, M.: Similarity law for Widom lines and coexistence lines. *Phys. Rev. E* **95**, 052120 (2017). <https://doi.org/10.1103/PhysRevE.95.052120>
57. Raju, M., Banuti, D.T., Ma, P.C., Ihme, M.: Widom Lines in Binary Mixtures of Supercritical Fluids. *Scientific Reports* **7**(1), 3027 (2017). <https://doi.org/10.1038/s41598-017-03334-3>
58. Chapman, S., Cowling, T.G.: *The Mathematical Theory of Non-uniform Gases*. Cambridge University Press, Cambridge (1970)
59. Ismail, A.F., Khulbe, K., Matsuura, T.: *Gas Separation Membranes—Polymeric and Inorganic*. Springer, Cham (2015). <https://doi.org/10.1007/978-3-319-01095-3>
60. Van der Bruggen, B., Schaep, J., Wilms, D., Vandecasteele, C.: Influence of molecular size, polarity and charge on the retention of organic molecules by nanofiltration. *J. Membr. Sci.* **156**(1), 29–41 (1999). [https://doi.org/10.1016/S0376-7388\(98\)00326-3](https://doi.org/10.1016/S0376-7388(98)00326-3)
61. van Leeuwen, M.E.: Derivation of Stockmayer potential parameters for polar fluids. *Fluid Phase Equilib.* **99**, 1–18 (1994). [https://doi.org/10.1016/0378-3812\(94\)80018-9](https://doi.org/10.1016/0378-3812(94)80018-9)

**Publisher's Note** Springer Nature remains neutral with regard to jurisdictional claims in published maps and institutional affiliations.